



Cite this: DOI: 10.1039/d6dt00496b

# High performing $Y_3H_5P_6O_{22}$ and $Er_3H_5P_6O_{22}$ proton conductors: preparation and conductivity study

Carlos M. R. Almeida,<sup>a,b</sup> Anatoly F. Selevich,<sup>c</sup> Laura I. V. Holz,<sup>a,b</sup>  
Francisco J. A. Loureiro<sup>a,b</sup> and Duncan P. Fagg<sup>a,b</sup>

Two novel trivalent rare-earth mixed-anion phosphates,  $Y_3H_5P_6O_{22}$  (YHPO) and  $Er_3H_5P_6O_{22}$  (EHPO), were synthesised using the thin layer technique (TLT) and processed into dense ceramic electrolytes via the cold sintering process (CSP). Structural characterisation by powder X-ray diffraction confirmed tetragonal symmetry for both compositions, with slight variations in lattice parameters consistent with ionic radius differences between  $Y^{3+}$  and  $Er^{3+}$ . Chemical analysis and infrared spectroscopy verified the coexistence of orthophosphate ( $PO_4^{3-}$ ) and pyrophosphate ( $P_2O_7^{4-}$ ) groups in a 1:1 molar ratio, forming hydrogen-bonded networks relevant to proton transport. The cold-sintered pellets exhibited high relative densities (>88%) and preserved stoichiometry. Electrochemical impedance spectroscopy performed between 40 °C and 140 °C under controlled wet ( $p_{H_2O} = 0.033$  atm) and low humidity ( $p_{H_2O} \sim 10^{-5}$  atm) nitrogen atmospheres revealed humidity-dependent proton conduction. Under wet conditions, two transport regimes were identified: a low-temperature vehicular mechanism associated with surface-adsorbed water and a higher-temperature thermally activated regime consistent with Grotthuss-type proton hopping. EHPO exhibited superior conductivity, reaching  $1.47 \times 10^{-4}$  S  $cm^{-1}$  at 140 °C, nearly one order of magnitude higher than YHPO. Under low humidity, both materials showed reduced conductivity and single Arrhenius-type behaviour with activation energies in the range of 50 kJ  $mol^{-1}$ –60 kJ  $mol^{-1}$ , indicating dominant structural proton diffusion. The enhanced performance of EHPO is attributed to its slightly more compact lattice, promoting favourable hydrogen-bond connectivity. These findings demonstrate the potential of trivalent rare-earth mixed phosphates as promising intermediate-temperature proton-conducting electrolytes.

Received 27th February 2026,  
Accepted 12th May 2026

DOI: 10.1039/d6dt00496b

rsc.li/dalton

## 1. Introduction

Proton-conducting ceramic devices have gained attention as a promising solution for clean and efficient energy conversion. Compared to conventional polymeric devices, notable benefits include higher operating temperatures, higher power density, greater fuel flexibility and relevance to chemical production.<sup>1</sup> A key factor in the performance of these devices is the development of high-efficiency electrolytes capable of conducting protons effectively at temperatures in the 200 °C–300 °C range, allowing such devices to be used in electrochemical synthesis of products such as ammonia and synthetic hydrocarbons.<sup>1–3</sup>

In this respect, metal phosphates (MPs) comprise a broad class of structurally versatile acidic solids with low cost, easy preparation and suitable thermal stability. These materials can be compositionally tailored to permit fast protonic conduction by the formation of hydrogen bonding networks or insertion of proton carriers, making these electrolytes attractive choices. As such, significant efforts have been dedicated to the synthesis and characterisation of metal phosphate-based proton conductors.<sup>4</sup> Among these, zirconium phosphates stand out due to the ability of Zr(IV) and phosphate ions to form a diverse range of crystallographic structures – from one-dimensional chains to three-dimensional open frameworks that can expand their functionality for electrochemical applications.<sup>4–6</sup> In addition, their ease of processing, environmental friendliness, and low cost further enhance their appeal. In contrast, other tetravalent phosphates and pyrophosphates, such as those based on Ti and Sn, have received less attention, largely due to their amorphous nature or tendency to become amorphous at operating temperatures.<sup>4,7,8</sup> Another standout metal

<sup>a</sup>TEMA – Centre for Mechanical Technology and Automation, Department of Mechanical Engineering, University of Aveiro, 3810-193 Aveiro, Portugal.

E-mail: francisco.loureiro@ua.pt, duncan@ua.pt

<sup>b</sup>LASI – Intelligent Systems Associate Laboratory, 4800-058 Guimarães, Portugal

<sup>c</sup>Research Institute for Physical Chemical Problems of the Belarusian State University, 220006 Minsk, Belarus. E-mail: selevich@bsu.by



phosphate material is the monovalent  $\text{CsH}_2\text{PO}_4$  compound that has shown strong performance as a superprotonic conducting electrolyte in both  $\text{H}_2/\text{O}_2$  and direct methanol fuel cells operating at around 240 °C. Moreover, combining  $\text{CsH}_2\text{PO}_4$  with other materials allows for the customisation of composite electrolytes, enabling a wide range of compositions with tailored properties.<sup>4,9</sup> Nonetheless, the electrochemical window of  $\text{CsH}_2\text{PO}_4$  is strongly limited by its decomposition at higher operating temperatures.

Recent advancements in metal phosphate proton conductors have increasingly focused on divalent and trivalent metal phosphates. These materials offer considerable structural versatility and adjustable conductivity.<sup>4</sup> However, they remain relatively understudied and further research is essential to fully evaluate their potential for application in low- and intermediate-temperature fuel cells. Among trivalent metal phosphates, the rare-earth phosphate family is particularly rich in structural diversity. The investigation of phase equilibria in these systems has historically been complicated by the viscous, barely stirrable nature of the phosphoric acid melts formed during synthesis, which prevented reliable equilibrium determination by conventional physicochemical analysis.<sup>10</sup> To overcome this limitation, the Thin Layer Technique (TLT) was developed, in which the reactive mixture is spread as a thin layer of 2 mm–5 mm thickness in a wide open crucible.<sup>10</sup> This geometry dramatically enhances the rate of evaporative dehydration and promotes rapid attainment of equilibrium without stirring, even in viscous or barely crystallising systems.<sup>10,11</sup> The TLT has since been applied systematically to the study of phase equilibria in these systems.<sup>10,11</sup> For the rare-earth series specifically, systematic investigation of phase equilibria in the  $\text{Ln}_2\text{O}_3\text{--P}_2\text{O}_5\text{--H}_2\text{O}$  systems ( $\text{Ln} = \text{La--Lu}$  and  $\text{Y}$ ) using the TLT has shown that a wide range of phosphate condensation states form sequentially as a function of temperature and water activity, from hydrated orthophosphates at low temperatures through diphosphates, triphosphates, tetraphosphates, polyphosphates and ultraphosphates at progressively higher temperatures.<sup>10,11</sup> A key finding of these studies is that, under TLT conditions with a moderate excess of phosphoric acid, the identity of the stable crystalline phase is determined primarily by temperature and relative humidity and is virtually independent of the exact  $\text{P}_2\text{O}_5 : \text{RE}_2\text{O}_3$  ratio across the range of  $(3\text{--}10) : 1$ .<sup>10,11</sup> For the heavier rare-earth elements and yttrium, the diphosphate  $\text{LnHP}_2\text{O}_7$  is the stable phase in the temperature range of 125 °C–150 °C, and mixed-anion phases containing both orthophosphate and pyrophosphate units have been identified as stable intermediates in several of these systems.<sup>11</sup>

In the present article, we, therefore, aim to introduce two new trivalent metal phosphates,  $\text{Er}_3\text{H}_5\text{P}_6\text{O}_{22}$  (EHPO) and  $\text{Y}_3\text{H}_5\text{P}_6\text{O}_{22}$  (YHPO). Here,  $\text{Y}^{3+}$  and  $\text{Er}^{3+}$  were specifically chosen due to their ability to form stable mixed-anion phases in the systematic TLT survey of the full lanthanide series.<sup>11</sup> Their placement in the crystallisation diagram is consistent with their ionic radius, with  $\text{Y}^{3+}$  ( $r^{(\text{VIII})} = 1.02 \text{ \AA}$ ) and  $\text{Er}^{3+}$  ( $r^{(\text{VIII})} = 1.00 \text{ \AA}$ ) being adjacent in the series.<sup>12</sup> These two elements, therefore, represent a closely matched pair within the heavy rare-earth

group, differing by only ~2% in ionic radius, which makes them ideal candidates for a controlled comparison of the effect of lattice parameter variation on the hydrogen-bond network geometry and proton transport properties of the resulting mixed-anion phosphate phases. Nonetheless, although  $\text{Y}^{3+}$  and  $\text{Er}^{3+}$  have similar ionic radii, the Er material is likely to be more ionic with higher basicity than the Y-analogue, potentially affecting its affinity for protonic charge carriers. Hence, in this work, we explore these two compositions, and we show how these materials can be synthesised by the thin layer technique (TLT) and processed into dense electrolyte materials by the cold sintering process (CSP). We then go on to examine the electrochemical performance of these materials as potential protonic electrolytes by performing electrochemical impedance spectroscopy (EIS) measurements under nitrogen atmospheres at different humidity levels ( $p_{\text{H}_2\text{O}} = 0.033 \text{ atm}$  and  $p_{\text{H}_2\text{O}} \sim 10^{-5} \text{ atm}$ ).

## 2. Experimental

### 2.1 Powder preparation and characterisation

The formation of  $\text{Er}_3\text{H}_5\text{P}_6\text{O}_{22}$  and  $\text{Y}_3\text{H}_5\text{P}_6\text{O}_{22}$  was established during the study of phase formation in  $\text{RE}_2\text{O}_3\text{--P}_2\text{O}_5\text{--H}_2\text{O}$  systems ( $\text{RE} = \text{Y, Er}$ ) using the thin layer technique (TLT). The TLT was developed previously to investigate phase equilibria in viscous, barely crystallising systems containing a volatile component ( $\text{H}_2\text{O}$ , in this case).<sup>10,11</sup> According to this technique, metal compounds react with phosphoric acid in a layer of 2–5 mm thickness of a solution or a flux. This peculiarity enhances the dehydration of the solution and promotes the quick attainment of the equilibrium state without stirring.

The starting materials were  $\text{Y}(\text{NO}_3)_3 \cdot 6\text{H}_2\text{O}$ ,  $\text{Er}(\text{NO}_3)_3 \cdot 5\text{H}_2\text{O}$  (Redkiymetall, Russia) and  $\text{H}_3\text{PO}_4$  (85%, Fine Chemicals, Belarus). All of them were reagent-grade products.

The initial homogeneous mixtures with a  $\text{P}_2\text{O}_5 : \text{RE}_2\text{O}_3$  molar ratio of 4 : 1 were placed in wide quartz or glassy carbon crucibles. This ratio was selected on the basis of the systematic TLT phase-equilibrium studies of the  $\text{Ln}_2\text{O}_3\text{--P}_2\text{O}_5\text{--H}_2\text{O}$  systems ( $\text{Ln} = \text{La--Lu}$  and  $\text{Y}$ ) previously performed across the complete range of  $\text{P}_2\text{O}_5 : \text{Ln}_2\text{O}_3 = (3\text{--}10) : 1$ .<sup>10,11</sup> A key result of those studies is that, under TLT conditions, the identity of the stable crystalline phase is governed primarily by temperature and relative humidity and is virtually independent of the exact  $\text{P}_2\text{O}_5 : \text{RE}_2\text{O}_3$  ratio across this range.<sup>10,11</sup> The 4 : 1 ratio was therefore chosen as the lower bound of the phosphate-rich regime validated for the heavier rare-earth systems, providing a twofold molar excess of phosphorus over the stoichiometric requirement of the target phase  $\text{RE}_3\text{H}_5\text{P}_6\text{O}_{22}$  (formal  $\text{P} : \text{RE} = 2 : 1$ ), while maintaining the acidic flux conditions necessary for the TLT to operate correctly. Next, the temperature was raised in a step mode with a step width of 25 °C up to 125 °C–150 °C and held for isothermal conditions for 2 weeks. The phase formation process was controlled by periodically studying samples using optical microscopy, since the crystals of the target substance had a specific shape in the form of a bevelled



prism. After intense crystallisation of the target compounds, the reaction mixtures were cooled. Crystalline phases were separated from the flux by washing with water using a glass filter and dried at room temperature.

Isolated compounds were identified by powder X-ray diffraction (PXRD), chemical analysis, quantitative thin-layer chromatography (QTLC) and thermal analysis. X-ray diffraction patterns were collected with a D8 ADVANCE powder diffractometer (Bruker AXS, Germany). The  $\text{CuK}\alpha$  radiation was selected by means of a Ni filter. The powder diffraction patterns were scanned in a step mode in the angular range  $10^\circ \leq 2\theta \leq 70^\circ$ , with  $t = 5$  s per step and  $\Delta 2\theta = 0.02^\circ$ . Analysis and indexing of the diffraction patterns were performed with the programs WinPLOTR<sup>13</sup> and DICVOL04.<sup>14</sup> The specific density of phosphates was determined pycnometrically. Standard procedures were used for chemical analysis of compounds. Yttrium and erbium were determined complexometrically with EDTA, while phosphorus was determined colourimetrically as the yellow phospho-vanadomolybdate complex.<sup>15</sup> The phosphate anions were identified by QTLC.<sup>16</sup> Simultaneous thermal analysis (STA) within the temperature range of 20 °C–1000 °C was carried out by using a NETZSCH STA 449C Jupiter (Germany) analyser at a heating rate of 10 °C  $\text{min}^{-1}$  under a nitrogen flow atmosphere.

## 2.2 Electrochemical cell fabrication and characterisation

Dense ceramic pellets were obtained by the cold sintering process (CSP) illustrated in Fig. 1,<sup>17,18</sup> where a slurry of the phosphates with water (80 wt% powder and 20 wt% deionized water) was held at 180 °C under 350 MPa of uniaxial pressure

for 75 min. The geometric dimensions and final masses of the pellets were: YHPO (area = 0.801  $\text{cm}^2$  and thickness = 0.220 cm, final mass = 0.507 g) and EHPO (area = 0.792  $\text{cm}^2$  and thickness = 0.125 cm, final mass = 360 g). The density of the pellets was measured at room temperature by the geometric method. After cold sintering, the surface top view microstructure was analysed using a tabletop scanning electron microscope (SEM, Hitachi SU-70). Energy-dispersive X-ray spectroscopy (EDS, Bruker SCU) was used to quantify elemental composition.

Spectroscopic studies in the mid infrared (MIR) region (400  $\text{cm}^{-1}$ –4000  $\text{cm}^{-1}$ ) were carried out using a Fourier transform infrared (FT-IR) spectrometer (Spectrum TWO LiTa, PerkinElmer; L1600300). The attenuated total reflectance Fourier transform infrared (ATR-FTIR) technique was used. The spectra were collected after 10 scans at 4  $\text{cm}^{-1}$  resolution.

Electrical characterisation of the prepared electrolytes was performed using AC electrochemical impedance spectroscopy (EIS). Symmetrical cells were assembled by applying silver electrodes (RS PRO 186-3600) to both sides of the electrolyte pellets, followed by a curing step in a ventilated oven at 135 °C for 10 min. Electrochemical measurements were carried out using an Autolab PGSTAT302N frequency response analyser over a frequency range of 0.1 Hz to 1 MHz with a signal amplitude of 50 mV. The measurements were conducted under a pure nitrogen atmosphere (flow rate = 50  $\text{mL min}^{-1}$ ) in two water vapour partial pressures to ensure both wet ( $p_{\text{H}_2\text{O}} = 0.033$  atm) and low humidity ( $p_{\text{H}_2\text{O}} \sim 10^{-5}$  atm) conditions. These levels of humidity were monitored using an online humidity sensor (JUMO). EIS measurements were collected at  $\sim 10$  °C intervals across a temperature range of  $\sim 40$  °C–140 °C, first in the direction of ascending temperature and subsequently in the direction of descending temperature. To ensure measurement stability and reproducibility, impedance spectra were recorded twice at each temperature point, allowing for a stabilisation period of 1 h between recordings. The impedance data were analysed with the complex nonlinear least squares (CNLS) fit program ZView 3.0 (Scribner Associates Inc., Southern Pines, NC, USA).

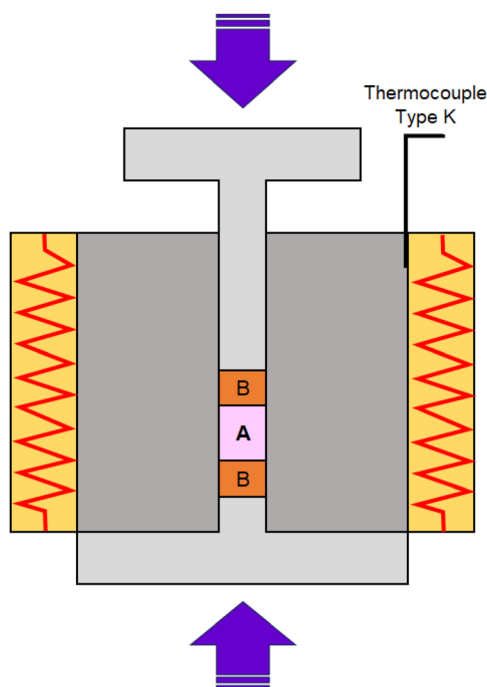


Fig. 1 Illustration of the cold sintering process, not to scale, where 'A' is the slurry to be pressed and 'B' represents 0.15 mm thick Kapton discs.

## 3. Results and discussion

### 3.1 Structural, thermal, and microstructural characterisation

Fig. 2a and b depict the powder X-ray diffraction (PXRD) patterns of the EHPO and the YHPO compounds obtained after CSP, along with the simulated patterns obtained for the precursor salts:  $\text{H}_3\text{PO}_4$  (PDF #00-025-0378),  $\text{Er}(\text{NO}_3)_3$  (PDF #01-083-4956), and  $\text{Y}(\text{NO}_3)_3$  (PDF #01-083-4951). Tables S1 and S2 show the indexed PXRD data of EHPO and YHPO compounds, respectively. Only one solution, the tetragonal system, was found. Values of  $M_N$  and  $F_N$  criteria ( $M_{20}/F_{20} = 89/96$ ,  $F_{39} = 60$  for  $\text{Y}_3\text{H}_5\text{P}_6\text{O}_{22}$ ;  $M_{20}/F_{20} = 81/104$ ,  $F_{47} = 95$  for  $\text{Er}_3\text{H}_5\text{P}_6\text{O}_{22}$ ) indicate that a reliable result has been obtained.<sup>19,20</sup> The absence of any discernible main reflections attributable to the corres-



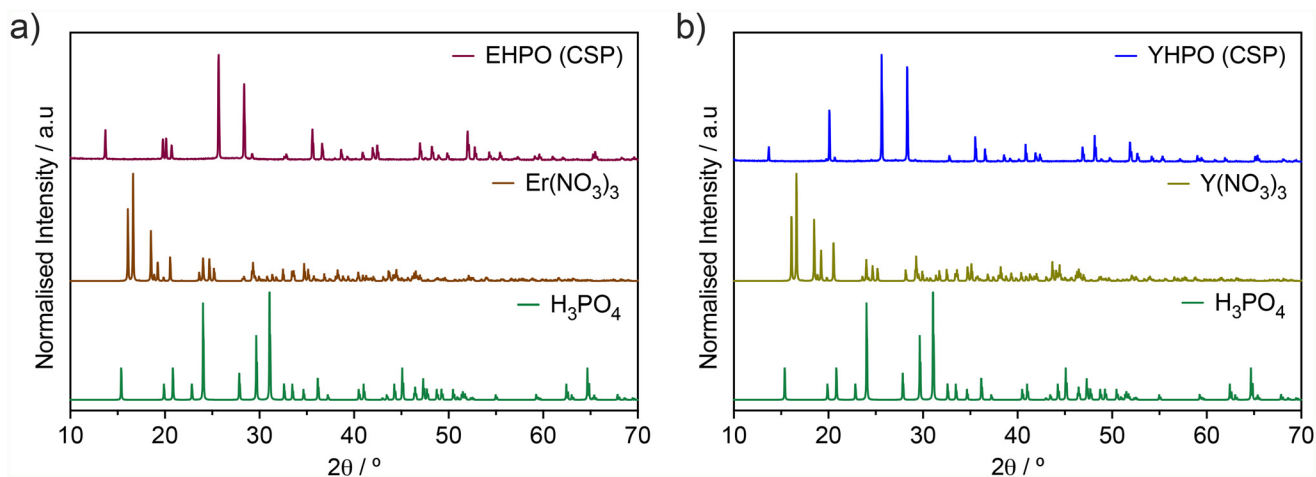


**Fig. 2** Powder X-ray diffraction (PXRD) patterns obtained for the synthesised (a) EHPO and (b) YHPO compounds obtained after CSP, along with the simulated patterns obtained for the precursor salts:  $\text{H}_3\text{PO}_4$ ,  $\text{Er}(\text{NO}_3)_3$ , and  $\text{Y}(\text{NO}_3)_3$ .

ponding precursor salt phases confirms the absence of residual precursor impurities.

Table 1 shows the obtained main crystallographic data (system, lattice parameters,  $a_{\text{cell}}$ ,  $c_{\text{cell}}$ , and unit cell volume,  $V_{\text{cell}}$ ) and the calculated ( $D_{\text{calc.}}$ ) and measured ( $D_{\text{meas.}}$ ) densities of the compounds. The determined unit cells enable the indexing of all the peaks in the Miller indices ( $hkl$ ) from powder diffraction patterns in Tables S1 and S2. All peaks were indexed to the tetragonal system. Notably, the unit cell lattice volume was found to be higher in the case of the YHPO sample ( $V_{\text{cell}} = 852.95 \text{ \AA}^3$ ), compared to that of the EHPO sample ( $V_{\text{cell}} = 847.31 \text{ \AA}^3$ ), in agreement with the larger effective ionic radius for  $\text{Y}^{3+}$  vs.  $\text{Er}^{3+}$ .<sup>12</sup> The identical tetragonal indexing, the isoformular compositions, and this regular lattice contraction collectively suggest that EHPO and YHPO are isostructural. In these metal phosphates, the observed differences in the relative intensities of certain reflections between the two PXRD patterns (Fig. 2a and b) are most likely attributed to preferred orientation effects arising during sample preparation for PXRD. Conversely, this difference in the lattice volume may play a crucial role in their electrical con-

ductivity by influencing the geometry and dynamics of charge carrier transport pathways.<sup>4</sup>

In accordance with thin layer technique (TLT) data, colourless  $\text{Y}_3\text{H}_5\text{P}_6\text{O}_{22}$  (YHPO) and light pink  $\text{Er}_3\text{H}_5(\text{P}_6\text{O}_{22})$  (EHPO) crystallise in the temperature range of 125–150 °C. Their crystals are shaped like skewed prisms. The results of chemical analysis presented in Table 2 show that the studied phosphates contain metal and phosphorus in a molar ratio of RE : P = 1 : 2. According to QTLC, the compounds are mixed-anion phosphates containing monophosphate and diphosphate anions in a molar ratio of  $\text{PO}_4^{3-} : \text{P}_2\text{O}_7^{4-} = 1 : 1$ , suggesting the general formula  $\text{Y}_3\text{H}_5(\text{PO}_4)_2(\text{P}_2\text{O}_7)_2$  (YHPO) and  $\text{Er}_3\text{H}_5(\text{PO}_4)_2(\text{P}_2\text{O}_7)_2$  (EHPO).

Simultaneous thermal analysis (STA) data, obtained up to 1000 °C, for the EHPO and the YHPO powder samples are given in Fig. 3a and b, respectively. As seen from the thermogravimetric analysis (TGA) curves, both compounds only show a minor weight loss of less than 0.5 wt% up to ~400 °C. This is accompanied by two small endothermic differential scanning calorimetry (DSC) peaks: the first one at a temperature of around 100 °C, which is likely due to the release of physi-

**Table 1** Main crystallographic data (system, lattice parameters,  $a_{\text{cell}}$ ,  $c_{\text{cell}}$ , and unit cell volume,  $V_{\text{cell}}$ ) of the synthesised compounds

Sample	System	$a/\text{\AA}$	$c/\text{\AA}$	$V_{\text{cell}}/\text{\AA}^3$	$D_{\text{calc.}}/\text{g cm}^{-3}$	$D_{\text{meas.}}/\text{g cm}^{-3}$	Z
YHPO	Tetragonal	6.9490(3)	17.6634(7)	852.95	3.15	3.12	2
EHPO	Tetragonal	6.9326(2)	17.6297(6)	847.31	4.10	4.06	2

**Table 2** Results of chemical analysis of the synthesised compounds

Sample Elements	YHPO			EHPO		
	Y	P	Y : P	Er	P	Er : P
Found, mass. %	33.11 ± 0.04	22.82 ± 0.08	1 : 1.98	48.12 ± 0.09	17.73 ± 0.07	1 : 1.99
Calc., mass. %	32.98	22.95	1 : 2	48.03	17.79	1 : 2



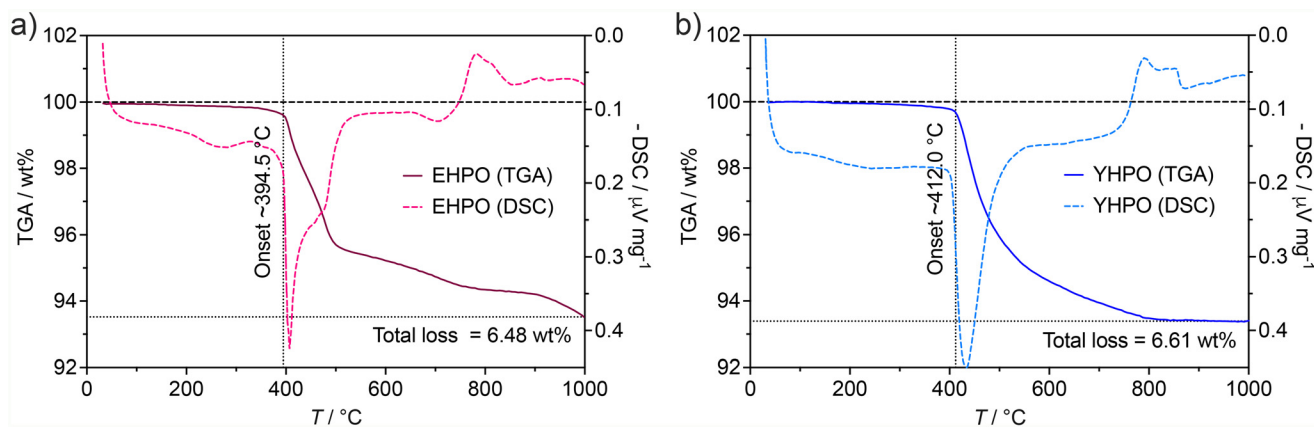


Fig. 3 Simultaneous thermal analysis (STA) data of (a) EHPO and (b) YHPO.

sorbed water on the powder surface,<sup>21,22</sup> and the second one at around 250 °C–270 °C, which may be due to the first step of the loss of crystallisation water.<sup>22</sup> This is followed by a large endothermic peak that is observed in the DSC curves of both samples, which coincides with the onset of thermal decomposition from the TGA curves (~394.5 °C for EHPO and ~412.0 °C for YHPO). This strong event that occurs in the temperature range of ~400–600 °C (DSC) can be ascribed to the complete dehydration process, where both metal phosphates decompose, losing constitutional water.<sup>21,22</sup> In accordance with PXRD data from Fig. 4, the final products of decomposition are mixtures of the corresponding tetragonal monophosphates, ErPO<sub>4</sub> (PDF #00-009-0383) and YPO<sub>4</sub> (PDF #01-091-4482), and monoclinic polyphosphates, Er(PO<sub>3</sub>)<sub>3</sub> (PDF #05-001-0191) and Y(PO<sub>3</sub>)<sub>3</sub> (PDF #05-001-0300), where these compounds start to crystallise at around 800 °C, corresponding to the exothermic DSC peaks observed above this temperature.

The FTIR spectra of the EHPO and YHPO powders are shown in Fig. 5, revealing key vibrational features associated

with phosphate (PO<sub>4</sub><sup>3-</sup>) and pyrophosphate (P<sub>2</sub>O<sub>7</sub><sup>4-</sup>) groups that are relevant to proton transport. Particular attention is given to the P–O and P–O–P stretching modes, which dominate the spectral region between ~1200 cm<sup>-1</sup> and ~700 cm<sup>-1</sup>.<sup>22–26</sup> This region is characterised by a series of broad and intense absorption bands, reflecting the complex vibrational behaviour of the phosphate framework. The PO<sub>4</sub><sup>3-</sup> groups feature only terminal P–O bonds, whereas the P<sub>2</sub>O<sub>7</sub><sup>4-</sup> groups comprise both terminal P–O bonds and characteristic bridging P–O–P bonds. Specifically, the bands at ~739 cm<sup>-1</sup> and ~900 cm<sup>-1</sup> are attributed to the symmetric ( $\nu_s$ ) and asymmetric ( $\nu_{as}$ ) stretching vibration of P–O–P bridges, respectively.<sup>23–25</sup> The peaks at ~993 cm<sup>-1</sup> and ~1190 cm<sup>-1</sup> can be assigned to the symmetric and asymmetric stretching modes of P–O bonds, respectively.<sup>23–25</sup> Additionally, a weak peak at ~1050 cm<sup>-1</sup> may be associated with the asymmetric P=O stretching vibration,  $\nu_{as}(\text{P}=\text{O})$ .<sup>26</sup>

The significant intensity of these features indicates that these groups are structurally dominant, in line with the results

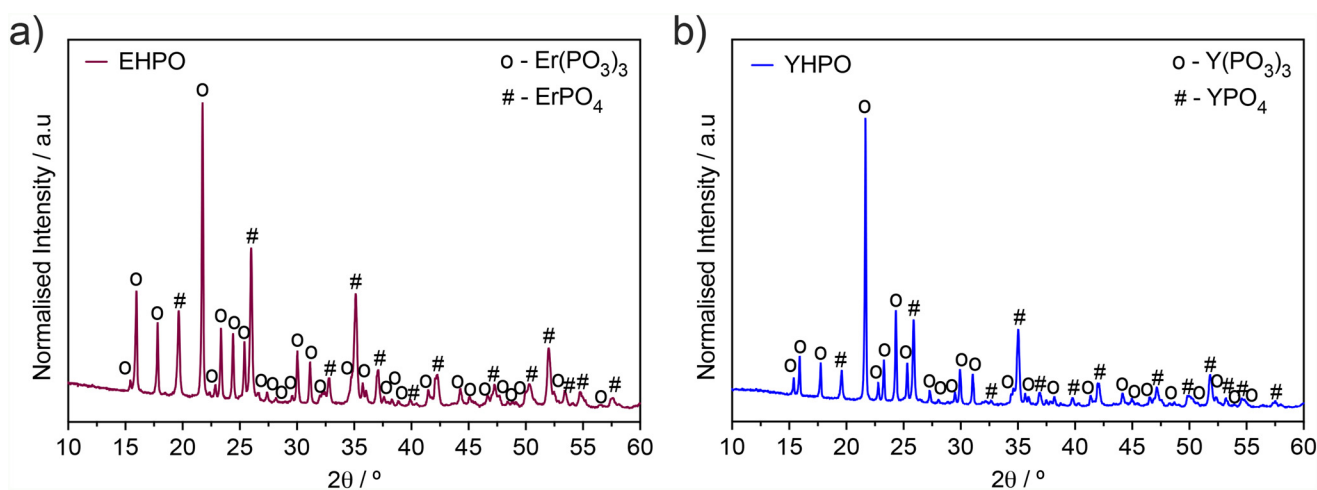


Fig. 4 Powder X-ray diffraction (PXRD) patterns obtained for the (a) EHPO and (b) YHPO compounds obtained after STA measurements up to 1000 °C.



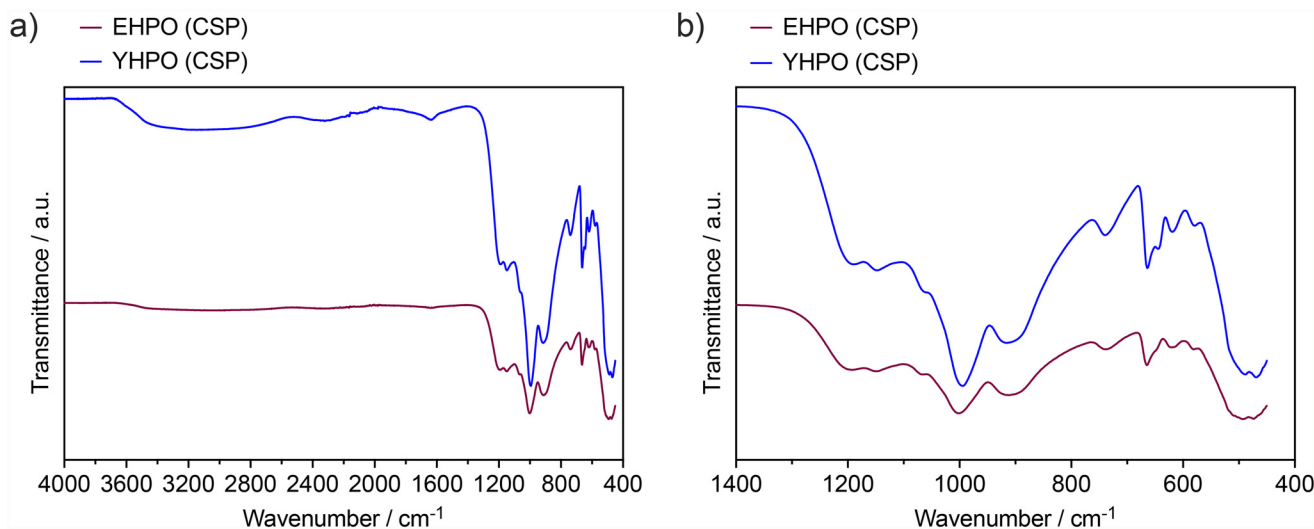


Fig. 5 (a) Fourier transform infrared (FTIR) spectra of the EHPO and the YHPO powders after CSP; (b) magnification within the  $1400\text{ cm}^{-1}$ – $400\text{ cm}^{-1}$  regions.

of chemical analysis and QTLC data for the synthesised metal phosphates. Meanwhile, the pronounced broadness of these peaks suggests a diversity of local bonding environments, likely arising from distortions or disorder within the crystal lattice.<sup>22</sup> Hydrogen bonding and partial protonation can also be visualised by the small absorbance around  $1650\text{ cm}^{-1}$ , which is an indication of P–O–H deformation mode, and also by the broad absorption band from  $2500\text{ cm}^{-1}$  to  $3500\text{ cm}^{-1}$ , which originates from the vibration of the O–H bond (PO–H or HO–H).<sup>23</sup> These structural effects are often correlated with enhanced proton mobility, as they contribute to the formation of a dynamic hydrogen-bond network.<sup>4,6,27,28</sup> In addition, these features are more pronounced in the EHPO sample, a factor that may have an impact on the electrochemical behaviour. Finally, below  $\sim 700\text{ cm}^{-1}$ , additional bands are observed that correspond to bending

modes, such as  $\delta(\text{P–O–P})$  and  $\delta(\text{O–P–O})$ , as well as symmetric stretching of metal–oxygen bonds,  $\nu_s(\text{M–O})$ ,<sup>25,29</sup> which in our work involves the rare-earth metal cations,  $\text{Er}^{3+}$  and  $\text{Y}^{3+}$ .

Fig. 6 illustrates the microstructure of the samples produced after cold sintering under identical conditions. All samples exhibit highly dense microstructures, in agreement with their measured relative densities of  $>88\%$ . Distinct bimodal grain size distributions can be observed varying between approximately  $4\text{ }\mu\text{m}$  and  $35\text{ }\mu\text{m}$  for YHPO and  $0.8\text{ }\mu\text{m}$  and  $5\text{ }\mu\text{m}$  for EHPO (higher magnification images are shown in Fig. S1). The origin of the bimodal crystallite size distribution observed by SEM is not fully understood at this stage. We note that the TLT synthesis produces crystals under conditions of progressive dehydration and stepwise temperature increase, which may favour successive crystallisation events. The RE:P

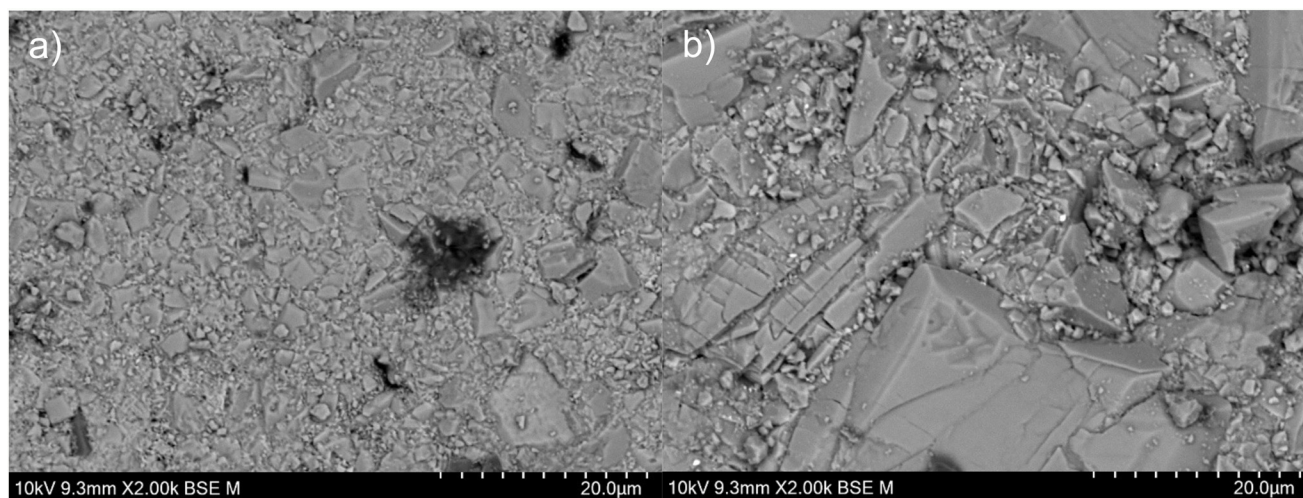


Fig. 6 Scanning electron microscopy (SEM) images obtained after cold sintering for (a) EHPO and (b) YHPO samples.



**Table 3** RE : P (RE – Y, Er) proportion obtained from energy-dispersive X-ray spectroscopy (EDS) analysis of the cold sintered pellets

Formula Elements	EHPO			YHPO		
	Er	P	Er : P	Y	P	Y : P
Atomic%	11.14 ± 2.24	20.64 ± 0.80	1 : 1.9	8.74 ± 1.25	20.16 ± 0.99	1 : 2.3

proportion after cold sintering, listed in Table 3 for both samples, is also in good agreement with the RE : P proportion of 1:2 quantified by chemical analysis, showing that the base compositions are not notably altered by the cold sintering process.

### 3.2 The effect of composition and humidity on the conductivity

The two metal phosphates were characterised by electrochemical impedance spectroscopy (EIS) to assess their electrical properties. Fig. 7 depicts examples of the impedance spectra collected under low humidity ( $p_{\text{H}_2\text{O}} \sim 10^{-5}$  atm) and wet ( $p_{\text{H}_2\text{O}} = 0.033$  atm)  $\text{N}_2$  conditions at 50 °C for both compositions. These spectra are representative of the entire studied temperature range (40–140 °C). In general, the data can be

noted to be composed of a depressed semicircle occurring in the high-frequency region and a low-frequency tail. However, in the case of YHPO measured under wet conditions, an additional depressed semicircle occurring at intermediate frequencies is visible. Therefore, the impedance responses were fitted with two or three parallel  $R\parallel\text{CPE}$  terms in series (Fig. 7), respectively. Here,  $R$  is the resistance ( $\Omega$ ) and CPE is a constant phase element, defined as

$$Z_{\text{CPE}} = Q^{-1}(i\omega)^{-n} \quad (1)$$

$\omega$  is the angular frequency, and  $Q$  and  $n$  are the usual parameters characterising the pseudo-capacitance and the exponent, respectively. The effective capacitance was calculated as

$$C = (RQ)^{1/n}(R)^{-1} \quad (2)$$

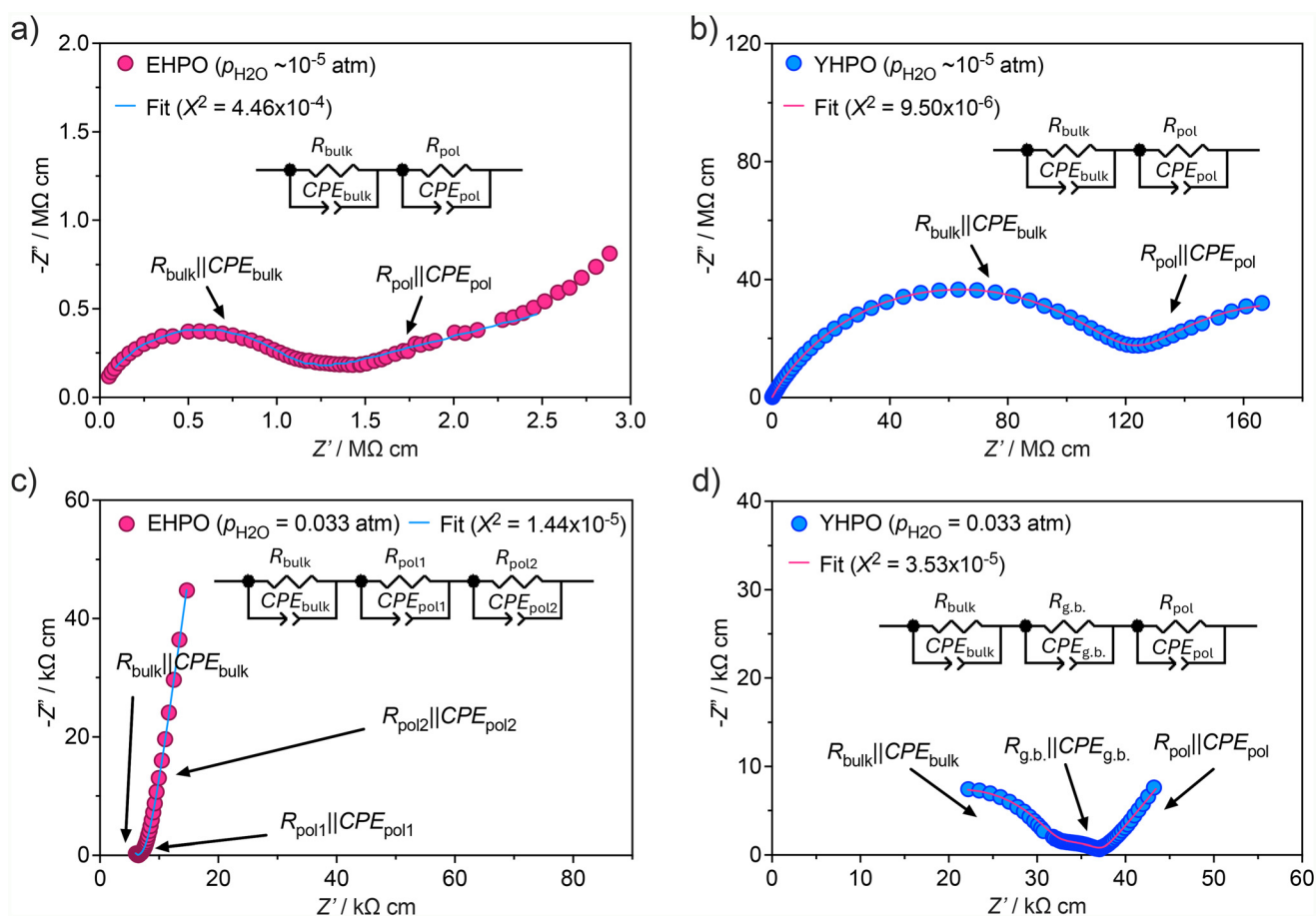


**Fig. 7** Electrochemical impedance spectroscopy (EIS) plots obtained at ~50 °C (heating cycle) under low humidity ( $p_{\text{H}_2\text{O}} \sim 10^{-5}$  atm)  $\text{N}_2$  for (a) EHPO and (b) YHPO; and under wet ( $p_{\text{H}_2\text{O}} = 0.033$  atm)  $\text{N}_2$  for (c) EHPO and (d) YHPO.



where  $Q$  and  $n$  are the usual parameters characterising the pseudo-capacitance.<sup>30,31</sup>

The high-frequency semicircle presents a capacitance in the range of  $\sim 10^{-12}$ – $10^{-11}$  F cm<sup>-1</sup>, characteristic of a bulk response ( $C_{\text{bulk}}$ ).<sup>30,31</sup> In the case of YHPO measured under wet conditions, the middle-frequency semicircle presents a capacitance of  $\sim 10^{-8}$  F cm<sup>-1</sup>, which is characteristic of a grain boundary response ( $C_{\text{g.b.}}$ ).<sup>30,31</sup> In contrast, the grain boundary semicircle is absent in EHPO under both wet and low humidity conditions. This phenomenon can be attributed to the short-circuiting of the grain boundaries: *i.e.*, if the grain boundaries become highly conductive, possibly due to additional conduction pathways such as parallel grain boundaries, they may not present a distinct impedance response.<sup>18,32</sup> In both cases, the low-frequency tail can be ascribed to the polarisation resistance, with an estimated capacitance ( $C_{\text{pol}}$ ) higher than  $10^{-6}$  F cm<sup>-2</sup>.<sup>30,31</sup>

The quality of the CNLS fits was assessed by the pseudo- $\chi^2$  criterion, with representative values obtained at  $\sim 50$  °C (heating cycle) ranging from  $10^{-6}$  to  $10^{-4}$  across all samples and atmospheric conditions (Fig. 7). The corresponding relative residuals plots are shown in Fig. 8, where both the real

( $\Delta_{\text{real}}$ ) and imaginary ( $\Delta_{\text{imag}}$ ) components remain within  $\pm 6\%$  across the measured frequency range. The Kramers–Kronig (KK) validation yielded values of  $\chi^2 \leq 10^{-5}$  across all conditions, confirming acceptable quality for the experimental data.<sup>33</sup>

Fig. 9 shows the temperature dependence of the total conductivity (bulk and grain boundary) obtained for both samples under both wet ( $p_{\text{H}_2\text{O}} = 0.033$  atm) and low humidity ( $p_{\text{H}_2\text{O}} \sim 10^{-5}$  atm) conditions. There are two noted regimes under wet conditions. The first occurs below  $\sim 100$  °C, where the total conductivity decreases with increasing temperature. This regime is typical of a vehicular transport mechanism, where a physisorbed water layer can promote the stabilisation of hydronium ions ( $\text{H}_3\text{O}^+$ ).<sup>34</sup> These protonated aqueous species provide a parallel, inter-grain pathway for fast protonic conduction along with the bulk conduction path.<sup>35,36</sup> As such, the impedance spectra do not resolve distinct bulk and grain-boundary semicircles. This is attributed to the exceptionally high proton conductivity along grain surfaces in the presence of adsorbed water, which renders the grain-boundary impedance contribution negligibly small relative to the bulk response and therefore indistinguishable in the complex impedance plane. In

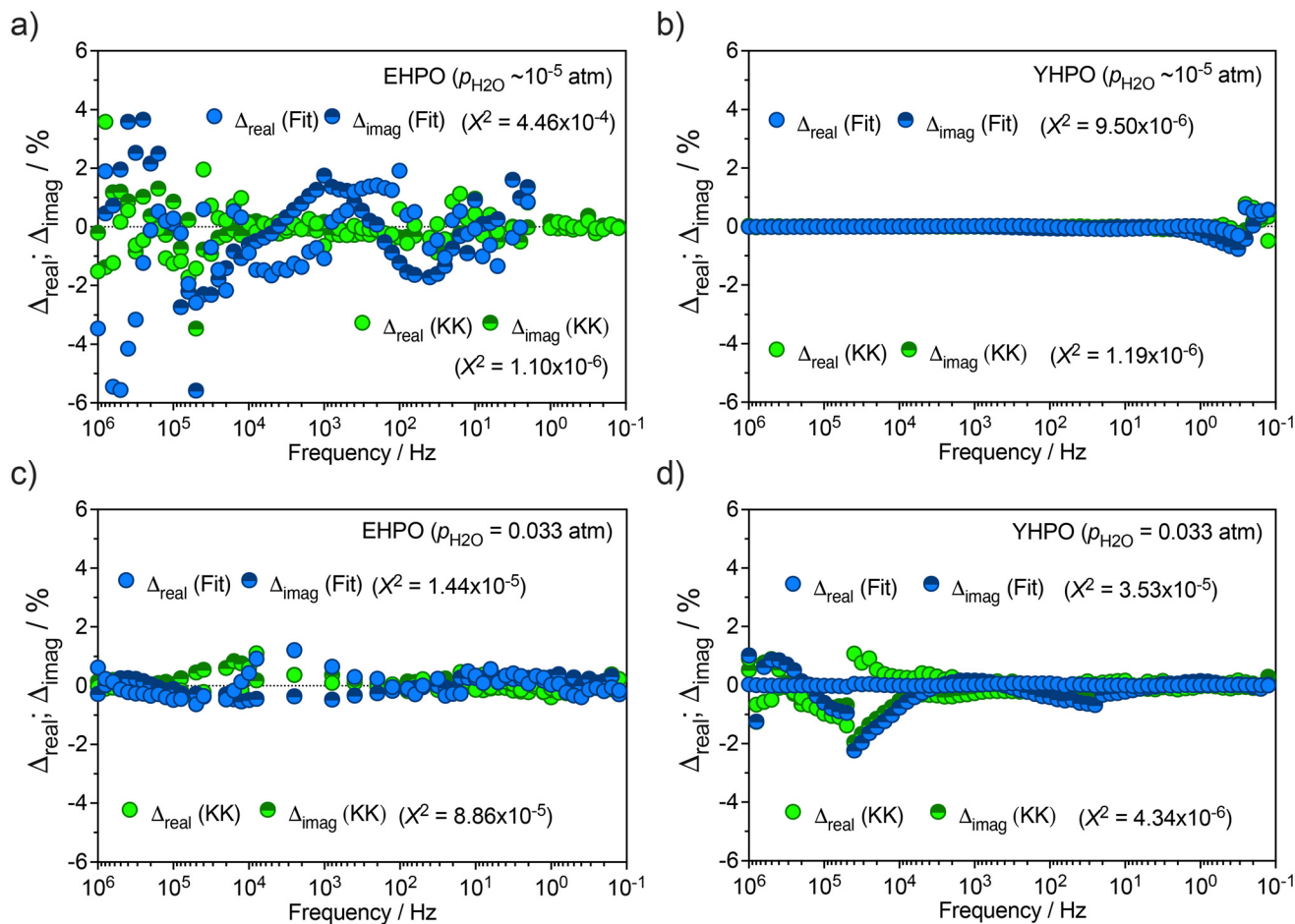


Fig. 8 Residual plots obtained from the EIS data at  $\sim 50$  °C (heating cycle) under low humidity ( $p_{\text{H}_2\text{O}} \sim 10^{-5}$  atm)  $\text{N}_2$  for (a) EHPO and (b) YHPO; and under wet ( $p_{\text{H}_2\text{O}} = 0.033$  atm)  $\text{N}_2$  for (c) EHPO and (d) YHPO.



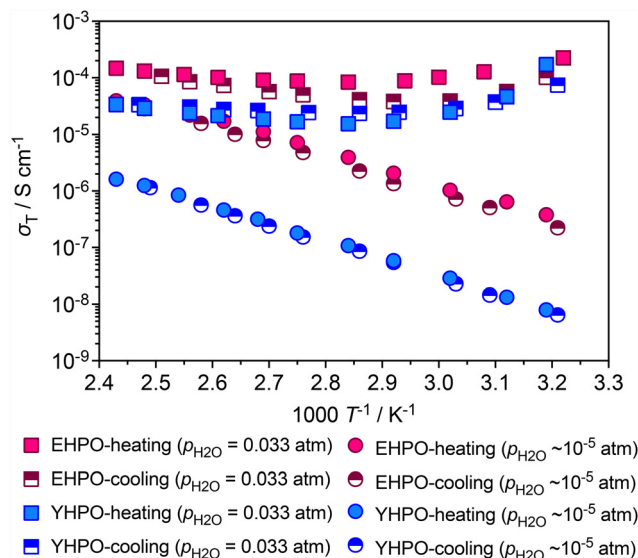


Fig. 9 The temperature dependence of the total conductivity obtained for the EHPO and YHPO samples.

this regime, the total conductivity slightly decreases with increasing temperature, possibly due to the loss or rearrangement of weakly bound surface water molecules as temperature increases. This progressive water loss reduces the availability of mobile proton carriers (*e.g.*,  $\text{H}_3\text{O}^+$ ) and weakens the connectivity of the hydrogen-bond network at the grain boundaries,<sup>34</sup> leading to a temporary decline in conductivity until 100 °C.

Conversely, as the temperature rises above ~100 °C, the total conductivity adopts a thermally activated behaviour, with a positive activation energy ( $E_a$ , Table 4). In this regime, low temperature, vehicular-type transport is expected to diminish due to dehydration of the physisorbed water layer (Fig. 3), and instead a new, thermally activated conduction process, such as the Grotthuss-type mechanism, becomes dominant.<sup>3,18,22,36</sup> This mechanism involves proton transfer along continuous hydrogen-bond networks within the phosphate lattice. The activation energy ( $E_a$ ) noted in this temperature regime for both samples (Table 4) is consistent with this type of mechanism at high relative humidity levels.<sup>34,37</sup> Therefore, the cross-over between these two regimes at ~100 °C is likely to reflect a transition from the dominance of a water-assisted surface conduction to intrinsic structural diffusion.

The significant scatter of the experimental points in Fig. 9 at low temperatures under wet conditions and the hysteresis

between the heating and cooling runs in this regime are a direct consequence of the mechanistic transition described above. In the temperature range below ~100 °C, the total conductivity is governed by the vehicular transport mechanism, which depends sensitively on the amount of adsorbed surface water. During the heating run, adsorbed water is progressively lost as temperature increases, gradually depleting the vehicular carrier concentration. During the subsequent cooling run, re-adsorption of water from the wet atmosphere occurs at a finite rate governed by the kinetics of surface adsorption, which does not precisely mirror the desorption process, eventually resulting in the observed hysteresis.<sup>18</sup> Above ~100 °C, where the Grotthuss-type structural diffusion mechanism dominates and the conductivity is no longer dependent on adsorbed water, the heating and cooling runs converge, and the scatter is correspondingly reduced.

Under these wet conditions, the total conductivity at ~140 °C reaches  $1.47 \times 10^{-4} \text{ S cm}^{-1}$  for EHPO, which is nearly an order of magnitude higher than that of YHPO ( $3.37 \times 10^{-5} \text{ S cm}^{-1}$ ) (Fig. 9). Structurally, YHPO is characterised by a larger lattice parameter compared to EHPO (Table 1). While we might expect that an expanded lattice would provide greater spatial freedom for proton transport, the increased lattice volume also would lead to longer O–O distances, particularly between hydrogen-bonded phosphate units.<sup>4,38</sup> Such extended O–O distances have been reported to potentially weaken the hydrogen bonding network in similar materials, reducing the likelihood of continuous proton-transfer pathways.<sup>4,38</sup> In contrast, EHPO exhibits a more compact unit cell (Table 1), which may help maintain optimal O–O distances to support continuous and flexible hydrogen bonding,<sup>27,39</sup> leading to the observed higher conduction of this composition. This balance can potentially promote the formation of dynamic hydrogen-bond networks with sufficient disorder and reorganisation ability, both of which are essential features of the Grotthuss mechanism.<sup>40</sup>

Importantly, under low humidity conditions, the total conductivity of both metal phosphate compositions is shown to decrease sharply, reflecting the strong dependence of their protonic transport on environmental water content. At ~140 °C, the total conductivity drops to  $3.91 \times 10^{-5} \text{ S cm}^{-1}$  for EHPO and  $1.62 \times 10^{-6} \text{ S cm}^{-1}$  for YHPO (both values being approximately one order of magnitude lower than their counterparts under wet conditions, Fig. 9). Moreover, under low humidity conditions, the temperature dependence of the total conductivity becomes more uniform, *i.e.*, both materials exhibit a continuous Arrhenius-type behaviour across the measured range (Fig. 9), with a single activation energy ( $E_a$ ) for protonic transport, as reported in Table 4. This contrasts with the behaviour under wet conditions, where two  $E_a$  regimes were observed, outlining the likely coexistence of different conduction pathways (*e.g.*, water-assisted *vs.* lattice-limited). The higher  $E_a$  values observed in low humidity (all in the range of ~50–60  $\text{kJ mol}^{-1}$ , Table 4) further support the notion that proton transport dominates the total conductivity at both humidity levels, but at lower  $p_{\text{H}_2\text{O}}$  values, it involves a higher

Table 4 Activation energy ( $E_a/\text{kJ mol}^{-1}$ ) values obtained for the EHPO and YHPO samples

Sample	Wet ( $p_{\text{H}_2\text{O}} = 0.033 \text{ atm}$ , $T > 100 \text{ °C}$ )		Dry ( $p_{\text{H}_2\text{O}} = 10^{-5} \text{ atm}$ , entire $T$ range)	
	Heating	Cooling	Heating	Cooling
EHPO	$18.47 \pm 0.93$	$31.80 \pm 1.54$	$55.12 \pm 1.37$	$58.48 \pm 0.76$
YHPO	$22.09 \pm 1.13$	$12.24 \pm 0.91$	$61.46 \pm 0.47$	$62.02 \pm 0.41$



energy barrier. In such cases, it seems reasonable to assume that a more significant part of the total conductivity is due to structural diffusion of protons within the bulk path under drier conditions and that the significant drop in conductivity between wet and low humidity conditions (Fig. 9) is due to a depletion in the number of protonic carriers.<sup>35,36</sup> This is corroborated with the FTIR spectra obtained after EIS measurements under low humidity conditions (Fig. 10). Here, the absorbance bands related to hydrogen bonding that were clearly observed in the spectra obtained after CSP (Fig. 5), e.g., at 1650  $\text{cm}^{-1}$  and from 2500  $\text{cm}^{-1}$  to 3500  $\text{cm}^{-1}$ , are now negligible, therefore, emphasising the role of water in protonation of the materials.

In the metal phosphate structures of YHPO and EHPO, both the orthophosphate ( $\text{PO}_4^{3-}$ ) and the pyrophosphate ( $\text{P}_2\text{O}_7^{4-}$ ) groups can retain protons as part of the crystal lattice. The  $\text{PO}_4^{3-}$  units can provide proton donor/acceptor groups (such as P–OH bonds), giving rise to small cavities where the lattice water is located. Although this water can form hydrogen bonds with the P–OH groups, an extended interlayer hydrogen bond network is unlikely under drier conditions. Therefore, it is more probable that a strong hydrogen-bond network is generated locally, particularly under conditions of low humidity.<sup>4,6,27</sup> In this regard, Ludueña *et al.*<sup>28</sup> proposed a carrier-mediated Grotthuss mechanism, in which water bridges the H-bond percolation path, complementing Grotthuss proton hopping between phosphonic acid groups. In this case, the Grotthuss-style hopping is supported by the short-distance transport of hydronium ions to neighbouring  $\text{PO}_4^{3-}$  tetrahedra. In contrast, the long-range transport of excess protons should be hindered by the low humidity.<sup>28</sup>

Considering the  $\text{P}_2\text{O}_7^{4-}$  groups, with their bridging oxygen atoms in P–O–P bonds, these could also enable longer-range connectivity and support the formation of extended proton-conducting pathways across the crystal lattice.<sup>41,42</sup> This could

be particularly relevant in drier environments, where vehicular transport (*i.e.*,  $\text{H}_3\text{O}^+$ -mediated movement) is unlikely. In such cases, structural diffusion would become the dominant mechanism, and the presence of  $\text{P}_2\text{O}_7^{4-}$  groups could ensure that protons are not isolated to local regions like in the P–OH groups, but may move through a percolating, continuous network. Another possibility is that both metal phosphates may retain some residual water as a result of condensation reactions.<sup>43–45</sup> In such a case, condensation products (P–O–P) may coexist with a certain amount of hydronium ions ( $\text{H}_3\text{O}^+$ ), albeit not of a concentration to be observable in the results of Fig. 10.

Further studies are, thus, necessary to shed more light on this discussion, as this possible multiple functionality may be the reason for proton conductivity to persist even under very low humidity conditions, albeit at lower magnitudes. Notably, the difference in conductivity between samples becomes more pronounced under low humidity, where EHPO maintains a relatively higher conductivity in the whole temperature range (Fig. 9). Again, this may emphasise the role of lattice volume in the formation of hydrogen bonding. In particular, the smaller lattice parameter of this sample may yield better-connected hydrogen-bond networks<sup>4,38</sup> and, thus, more efficient proton transport.

Finally, the FTIR spectra recorded after the EIS measurements (Fig. 10) also reveal partial attenuation of bands in the 650  $\text{cm}^{-1}$ –450  $\text{cm}^{-1}$  region, which are assigned to the bending vibrations of terminal  $\text{PO}_3$  groups.<sup>25</sup> This change is tentatively attributed to partial condensation of P–OH groups within the phosphate network during the thermal and humidity cycling of the impedance measurements, consistent with the dynamic participation of the hydrogen-bond network in proton transport discussed above. Nonetheless, the post-measurement PXRD patterns (Fig. S2) confirm that the bulk crystal structure is preserved, indicating that this reorganisation is confined to

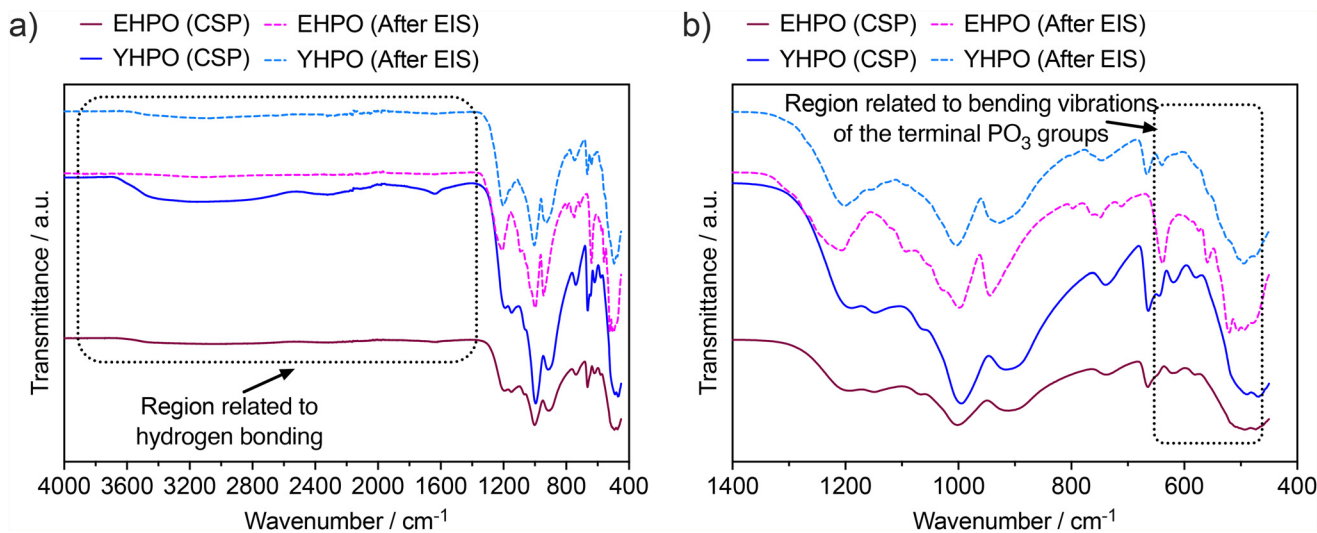


Fig. 10 (a) Fourier transform infrared (FTIR) spectra of the EHPO and YHPO powders after EIS along with the data obtained after CSP from Fig. 5 under low humidity conditions ( $p_{\text{H}_2\text{O}} \sim 10^{-5}$  atm); (b) magnification within the 1400  $\text{cm}^{-1}$ –400  $\text{cm}^{-1}$  regions.



the local hydrogen-bonding environment of the phosphate groups rather than representing a phase transformation.

## 4. Conclusions

Two new trivalent rare-earth mixed orthophosphate–pyrophosphate compounds,  $Y_3H_5(PO_4)_2(P_2O_7)_2$  (YHPO) and  $Er_3H_5(PO_4)_2(P_2O_7)_2$  (EHPO), were successfully synthesised by the thin layer technique and densified using the cold sintering process, yielding highly compact ceramic electrolytes without significant compositional alteration. Both materials crystallise in the tetragonal system and contain mixed phosphate anions that support hydrogen bonding and proton mobility.

Electrochemical analysis demonstrated clear humidity-dependent proton transport behaviour. Under wet conditions, conductivity is enhanced by surface-assisted vehicular transport below  $\sim 100$  °C, followed by thermally activated Grotthuss-type structural diffusion at higher temperatures. Under low humidity, conductivity decreases significantly and exhibits a single Arrhenius behaviour with higher activation energies, indicating dominant bulk structural diffusion with limited contribution from water-mediated pathways.

Among the two compositions, EHPO consistently exhibited superior conductivity, particularly under wet conditions, reaching  $1.47 \times 10^{-4}$  S  $cm^{-1}$  at 140 °C. The improved performance is attributed to its slightly smaller lattice volume, which likely favours stronger and more continuous hydrogen-bond networks, facilitating long-range proton transport. However, the performance exhibited by the EHPO compounds is notably superior to that reported for the well-established superprotonic conductor  $CsH_2PO_4$ , which exhibits a total conductivity of the order of  $10^{-5}$  S  $cm^{-1}$  under significantly higher water vapour partial pressures ( $p_{H_2O} \sim 10^{-1}$  atm),<sup>9,18,46</sup> highlighting the promising performance of these mixed rare-earth phosphates as intermediate-temperature proton-conducting electrolytes.

The present study establishes the synthesis, structural characterisation and initial electrochemical performance of EHPO and YHPO as a foundation for future development. Overall, this work highlights the structural and functional relevance of mixed-anion rare-earth phosphates and demonstrates that subtle crystallographic differences can significantly influence proton conduction. These materials represent promising candidates for further development as intermediate-temperature proton-conducting electrolytes, particularly where moderate humidity conditions can be maintained. Key targets for subsequent work include determination of the thermal expansion coefficients of both compounds to assess thermomechanical compatibility with electrode materials, fabrication and testing of complete electrochemical devices, and long-term stability evaluation under sustained operation. The structural integrity of both materials after the impedance measurements conducted here has been confirmed by post-measurement PXRD, providing an encouraging preliminary indication of stability under the conditions employed.

## Conflicts of interest

There are no conflicts to declare.

## Data availability

The authors declare that the data supporting the findings of this study are available from the corresponding authors upon reasonable request.

Supplementary information (SI) is available. See DOI: <https://doi.org/10.1039/d6dt00496b>.

## Acknowledgements

The authors acknowledge the grants/projects with references: 2023.05868.CEECIND, 2020.02797.CEECIND/CP1589/CT0030 (<https://doi.org/10.54499/2020.02797.CEECIND/CP1589/CT0030>), 2022.09319.PTDC (<https://doi.org/10.54499/2022.09319.PTDC>), 2022.02498.PTDC (<https://doi.org/10.54499/2022.02498.PTDC>), COMPETE2030-FEDER-00744500 16284 2023.17866.ICDT (<https://doi.org/10.54499/2023.17866.ICDT>), COMPETE2030-FEDER-00770000, CENTRO2030-FEDER-02363200, 2024.14251.PEX (<https://doi.org/10.54499/2024.14251.PEX>) and UID 00481/2025 – Centre for Mechanical Technology and Automation (<https://doi.org/10.54499/UID/00481/2025>) from Fundação para a Ciência e a Tecnologia (FCT). In addition, the authors acknowledge the State Scientific Research Program of Belarus “Chemical processes, reagents and technologies, bioregulators and bioorganic chemistry”, 2021–2025, project Himreagent-2.1.07.2.

## References

- 1 Y. Wang, Y. Ling, B. Wang, G. Zhai, G. Yang, Z. Shao, *et al.*, A review of progress in proton ceramic electrochemical cells: material and structural design, coupled with value-added chemical production, *Energy Environ. Sci.*, 2023, **16**, 5721–5770, DOI: [10.1039/D3EE03121G](https://doi.org/10.1039/D3EE03121G).
- 2 B. Wang, T. Li, F. Gong, M. H. D. Othman and R. Xiao, Ammonia as a green energy carrier: Electrochemical synthesis and direct ammonia fuel cell - a comprehensive review, *Fuel Process. Technol.*, 2022, **235**, 107380, DOI: [10.1016/j.fuproc.2022.107380](https://doi.org/10.1016/j.fuproc.2022.107380).
- 3 F. J. A. Loureiro, D. Pérez-Coll, V. C. D. Graça, S. M. Mikhalev, A. F. G. Ribeiro, A. Mendes, *et al.*, Proton conductivity in yttrium-doped barium cerate in nominally dry reducing conditions for application in chemical synthesis, *J. Mater. Chem. A*, 2019, **7**, 18135–18142, DOI: [10.1039/C9TA04584H](https://doi.org/10.1039/C9TA04584H).
- 4 R. M. P. Colodrero, P. Olivera-Pastor, A. Cabeza and M. Bazaga-García, Properties and Applications of Metal Phosphates and Pyrophosphates as Proton Conductors, *Materials*, 2022, **15**(4), 1292, DOI: [10.3390/ma15041292](https://doi.org/10.3390/ma15041292).
- 5 A. Clearfield and S. D. Smith, The crystal structure of zirconium phosphate and the mechanism of its ion exchange behavior, *J. Colloid Interface Sci.*, 1968, **28**, 325–330, DOI: [10.1016/0021-9797\(68\)90136-7](https://doi.org/10.1016/0021-9797(68)90136-7).



- 6 A. Clearfield and G. D. Smith, Crystallography and structure of .alpha.-zirconium bis(monohydrogen orthophosphate) monohydrate, *Inorg. Chem.*, 1969, **8**, 431–436, DOI: [10.1021/ic50073a005](https://doi.org/10.1021/ic50073a005).
- 7 T. Anfimova, T. Lie-Andersen, E. P. Jensen, C. B. Prag, U. G. Nielsen, D. R. Sørensen, *et al.*, The effect of preparation method on the proton conductivity of indium doped tin pyrophosphates, *Solid State Ion.*, 2015, **278**, 209–216, DOI: [10.1016/j.ssi.2015.06.021](https://doi.org/10.1016/j.ssi.2015.06.021).
- 8 W. H. J. Hogarth, S. S. Muir, A. K. Whittaker, J. C. Diniz da Costa, J. Drennan and G. Q. Lu, Max. Proton conduction mechanism and the stability of sol-gel titanium phosphates, *Solid State Ion.*, 2007, **177**, 3389–3394, DOI: [10.1016/j.ssi.2006.10.015](https://doi.org/10.1016/j.ssi.2006.10.015).
- 9 S. M. Haile, C. R. I. Chisholm, K. Sasaki, D. A. Boysen and T. Uda, Solid acid proton conductors: from laboratory curiosities to fuel cell electrolytes, *Faraday Discuss.*, 2007, **134**, 17–39, DOI: [10.1039/B604311A](https://doi.org/10.1039/B604311A).
- 10 A. F. Selevich and A. I. Lesnikovich, Interactions in the Mn<sub>2</sub>O<sub>3</sub>-P<sub>2</sub>O<sub>5</sub>-H<sub>2</sub>O System by the Thin-Layer Technique, *Russ. J. Inorg. Chem.*, 1994, **39**, 1322–1326.
- 11 A. F. Selevich, A. S. Lyakhov and A. I. Lesnikovich, Phase equilibrium in the systems Ln<sub>2</sub>O<sub>3</sub> - P<sub>2</sub>O<sub>5</sub> - H<sub>2</sub>O: Regularities of formation and some properties of rare earth phosphates, *Phosphorus Res. Bull.*, 1999, **10**, 171–176, DOI: [10.3363/prb1992.10.0\\_171](https://doi.org/10.3363/prb1992.10.0_171).
- 12 R. D. Shannon, Revised effective ionic radii and systematic studies of interatomic distances in halides and chalcogenides, *Acta Crystallogr., Sect. A*, 1976, **32**, 751–767, DOI: [10.1107/S0567739476001551](https://doi.org/10.1107/S0567739476001551).
- 13 T. Roisnel and J. Rodríguez-Carvajal, WinPLOTR: A Windows Tool for Powder Diffraction Pattern Analysis, *Mater. Sci. Forum*, 2001, **378–381**, 118–123, DOI: [10.4028/www.scientific.net/MSF.378-381.118](https://doi.org/10.4028/www.scientific.net/MSF.378-381.118).
- 14 A. Boultif and D. Louër, Powder pattern indexing with the dichotomy method, *J. Appl. Crystallogr.*, 2004, **37**, 724–731, DOI: [10.1107/S0021889804014876](https://doi.org/10.1107/S0021889804014876).
- 15 G. Charlot, *Les méthodes de la chimie analytique, analyse quantitative minérale*, 5e éd., Paris SE - x, 1024 pages illustrations 25 cm: Masson et Cie, 1966. <https://worldcat.org/title/17428642>.
- 16 E. A. Prodan, I. L. Shashkova and T. N. Galkova, Effect of cations on the separation of phosphates by thin layer chromatography, *Zh. Anal. Khim.*, 1978, **33**, 2304–2309.
- 17 C. Vakifahmetoglu and L. Karacasulu, Cold sintering of ceramics and glasses: A review, *Curr. Opin. Solid State Mater. Sci.*, 2020, **24**, 100807, DOI: [10.1016/j.cossms.2020.100807](https://doi.org/10.1016/j.cossms.2020.100807).
- 18 B. M. G. Melo, F. J. A. Loureiro, S. M. Mikhalev, D. P. Fagg, L. C. Costa and M. P. F. Graça, Alternative processing routes on CsH<sub>2</sub>PO<sub>4</sub> proton conductors: Cold sintering and ball-milling routes, *Int. J. Hydrogen Energy*, 2024, **73**, 736–748, DOI: [10.1016/j.ijhydene.2024.06.077](https://doi.org/10.1016/j.ijhydene.2024.06.077).
- 19 P. M. De Wolff, A simplified criterion for the reliability of a powder pattern indexing, *J. Appl. Crystallogr.*, 1968, **1**, 108–113, DOI: [10.1107/S002188986800508X](https://doi.org/10.1107/S002188986800508X).
- 20 G. S. Smith and R. L. Snyder, FN: A criterion for rating powder diffraction patterns and evaluating the reliability of powder-pattern indexing, *J. Appl. Crystallogr.*, 1979, **12**, 60–65, DOI: [10.1107/S002188987901178X](https://doi.org/10.1107/S002188987901178X).
- 21 P. Singh, A. K. Sharma and P. Kumar, Phase, porosity, and conductivity analysis of RbH<sub>2</sub>PO<sub>4</sub>/CeP<sub>2</sub>O<sub>7</sub> nanocomposites, *Ionics*, 2025, **31**, 2291–2301, DOI: [10.1007/s11581-024-06035-w](https://doi.org/10.1007/s11581-024-06035-w).
- 22 Y. Matsuda, N. Ueda, K. Funakoshi, J. Nakajima, D. Mori, S. Taminato, *et al.*, Proton conductivity in mixed cation phosphate, KMg<sub>1-x</sub>H<sub>2x</sub>(PO<sub>3</sub>)<sub>y</sub>H<sub>2</sub>O, with a layered structure at low-intermediate temperatures, *Dalton Trans.*, 2021, **50**, 7678–7685, DOI: [10.1039/D1DT01187A](https://doi.org/10.1039/D1DT01187A).
- 23 X. Xu, S. Tao, P. Wormald and J. T. S. Irvine, Intermediate temperature stable proton conductors based upon SnP<sub>2</sub>O<sub>7</sub>, including additional H<sub>3</sub>PO<sub>4</sub>, *J. Mater. Chem.*, 2010, **20**, 7827–7833, DOI: [10.1039/C0JM01089H](https://doi.org/10.1039/C0JM01089H).
- 24 P. S. Attidekou, P. A. Connor, P. Wormald, D. P. Tunstall, S. M. Francis and J. T. S. Irvine, Solid state NMR studies of phosphate/tin matrix formed on electrochemical insertion into SnP<sub>2</sub>O<sub>7</sub>, *Solid State Ion.*, 2004, **175**, 185–190, DOI: [10.1016/j.ssi.2003.12.048](https://doi.org/10.1016/j.ssi.2003.12.048).
- 25 M. Gabelica-Robert and P. Tarte, Infrared spectrum of crystalline and glassy pyrophosphates : preservation of the pyrophosphate group in the glassy structure, *J. Mol. Struct.*, 1982, **79**, 251–254, DOI: [10.1016/0022-2860\(82\)85061-8](https://doi.org/10.1016/0022-2860(82)85061-8).
- 26 H. Patel and U. Chudasama, A comparative study of proton transport properties of metal (IV) phosphates, *J. Chem. Sci.*, 2007, **119**, 35–40, DOI: [10.1007/s12039-007-0006-8](https://doi.org/10.1007/s12039-007-0006-8).
- 27 T. Ogawa, H. Ushiyama, J.-M. Lee, T. Yamaguchi and K. Yamashita, Theoretical Studies on Proton Transfer among a High Density of Acid Groups: Surface of Zirconium Phosphate with Adsorbed Water Molecules, *J. Phys. Chem. C*, 2011, **115**, 5599–5606, DOI: [10.1021/jp107767d](https://doi.org/10.1021/jp107767d).
- 28 G. A. Ludueña, T. D. Kühne and D. Sebastiani, Mixed Grotthuss and Vehicle Transport Mechanism in Proton Conducting Polymers from Ab initio Molecular Dynamics Simulations, *Chem. Mater.*, 2011, **23**, 1424–1429, DOI: [10.1021/cm102674u](https://doi.org/10.1021/cm102674u).
- 29 R. Hubin and P. Tarte, Spectre d'absorption infra-rouge des pyrophosphates et pyroarséniates cubiques d'éléments tétravalents X<sub>IV</sub>P<sub>2</sub>O<sub>7</sub> et X<sub>IV</sub>As<sub>2</sub>O<sub>7</sub>, *Spectrochim. Acta, Part A*, 1967, **23**, 1815–1829, DOI: [10.1016/0584-8539\(67\)80064-3](https://doi.org/10.1016/0584-8539(67)80064-3).
- 30 J. T. S. Irvine, D. C. Sinclair and A. R. West, Electroceramics: Characterization by Impedance Spectroscopy, *Adv. Mater.*, 1990, **2**, 132–138, DOI: [10.1002/adma.1990020304](https://doi.org/10.1002/adma.1990020304).
- 31 N. Nasani, P. A. N. Dias, J. A. Saraiva and D. P. Fagg, Synthesis and conductivity of Ba(Ce,Zr,Y)O<sub>3-δ</sub> electrolytes for PCFCs by new nitrate-free combustion method, *Int. J. Hydrogen Energy*, 2013, **38**, 8461–8470, DOI: [10.1016/j.ijhydene.2013.04.078](https://doi.org/10.1016/j.ijhydene.2013.04.078).
- 32 N. J. Kidner, N. H. Perry, T. O. Mason and E. J. Garboczi, The Brick Layer Model Revisited: Introducing the Nano-



- Grain Composite Model, *J. Am. Ceram. Soc.*, 2008, **91**, 1733–1746, DOI: [10.1111/j.1551-2916.2008.02445.x](https://doi.org/10.1111/j.1551-2916.2008.02445.x).
- 33 B. A. Boukamp, Guidance to solid state electrochemical impedance spectroscopy, *Electrochim. Acta*, 2025, **537**, 146892, DOI: [10.1016/j.electacta.2025.146892](https://doi.org/10.1016/j.electacta.2025.146892).
- 34 J.-P. Melchior, K.-D. Kreuer and J. Maier, Proton conduction mechanisms in the phosphoric acid–water system ( $\text{H}_4\text{P}_2\text{O}_7\text{--H}_3\text{PO}_4\cdot 2\text{H}_2\text{O}$ ): a  $^1\text{H}$ ,  $^{31}\text{P}$  and  $^{17}\text{O}$  PFG-NMR and conductivity study, *Phys. Chem. Chem. Phys.*, 2017, **19**, 587–600, DOI: [10.1039/C6CP04855B](https://doi.org/10.1039/C6CP04855B).
- 35 D. B. Asay and S. H. Kim, Evolution of the Adsorbed Water Layer Structure on Silicon Oxide at Room Temperature, *J. Phys. Chem. B*, 2005, **109**, 16760–16763, DOI: [10.1021/jp053042o](https://doi.org/10.1021/jp053042o).
- 36 S.Ø Stub, E. Vøllestad and T. Norby, Mechanisms of Protonic Surface Transport in Porous Oxides: Example of YSZ, *J. Phys. Chem. C*, 2017, **121**, 12817–12825, DOI: [10.1021/acs.jpcc.7b03005](https://doi.org/10.1021/acs.jpcc.7b03005).
- 37 Y. Aihara, A. Sonai, M. Hattori and K. Hayamizu, Ion Conduction Mechanisms and Thermal Properties of Hydrated and Anhydrous Phosphoric Acids Studied with  $^1\text{H}$ ,  $^2\text{H}$ , and  $^{31}\text{P}$  NMR, *J. Phys. Chem. B*, 2006, **110**, 24999–25006, DOI: [10.1021/jp064452v](https://doi.org/10.1021/jp064452v).
- 38 K. Zhang, M. Ji, X.-Y. Zhou, F. Xuan, B. Duan, Y. Yuan, *et al.*, The proton conduction behavior of two 1D open-framework metal phosphates with similar crystal structures and different hydrogen bond networks, *RSC Adv.*, 2023, **13**, 12703–12711, DOI: [10.1039/D3RA01130E](https://doi.org/10.1039/D3RA01130E).
- 39 T. Anfimova, Q. Li, J. O. Jensen and N. J. Bjerrum, Thermal Stability and Proton Conductivity of Rare Earth Orthophosphate Hydrates, *Int. J. Electrochem. Sci.*, 2014, **9**, 2285–2300, DOI: [10.1016/S1452-3981\(23\)07927-0](https://doi.org/10.1016/S1452-3981(23)07927-0).
- 40 P. Žguncs, K. Klyukin, L. S. Wang, G. Xiong, J. Li, S. M. Haile, *et al.*, Uncovering fast solid-acid proton conductors based on dynamics of polyanion groups and proton bonding strength, *Energy Environ. Sci.*, 2024, **17**, 5730–5742, DOI: [10.1039/D4EE01219D](https://doi.org/10.1039/D4EE01219D).
- 41 G. Y. Foran and G. R. Goward, Site-Specific Proton Dynamics in Indium-Doped Tin Pyrophosphate, *J. Phys. Chem. C*, 2020, **124**, 28407–28416, DOI: [10.1021/acs.jpcc.0c09290](https://doi.org/10.1021/acs.jpcc.0c09290).
- 42 Y. Sato, Y. Shen, M. Nishida, W. Kanematsu and T. Hibino, Proton conduction in non-doped and acceptor-doped metal pyrophosphate ( $\text{MP}_2\text{O}_7$ ) composite ceramics at intermediate temperatures, *J. Mater. Chem.*, 2012, **22**, 3973–3981, DOI: [10.1039/C2JM15335A](https://doi.org/10.1039/C2JM15335A).
- 43 A. Kaltbeitzel, S. Schauff, H. Steininger, B. Bingöl, G. Brunklaus, W. H. Meyer, *et al.*, Water sorption of poly(vinylphosphonic acid) and its influence on proton conductivity, *Solid State Ion.*, 2007, **178**, 469–474, DOI: [10.1016/j.ssi.2007.02.007](https://doi.org/10.1016/j.ssi.2007.02.007).
- 44 H. Steininger, M. Schuster, K. D. Kreuer, A. Kaltbeitzel, B. Bingöl, W. H. Meyer, *et al.*, Intermediate temperature proton conductors for PEM fuel cells based on phosphonic acid as protogenic group: A progress report, *Phys. Chem. Chem. Phys.*, 2007, **9**, 1764–1773, DOI: [10.1039/B618686F](https://doi.org/10.1039/B618686F).
- 45 M. Schuster, K.-D. Kreuer, H. Steininger and J. Maier, Proton conductivity and diffusion study of molten phosphonic acid  $\text{H}_3\text{PO}_3$ , *Solid State Ion.*, 2008, **179**, 523–528, DOI: [10.1016/j.ssi.2008.03.030](https://doi.org/10.1016/j.ssi.2008.03.030).
- 46 A. Ishikawa, H. Maekawa, T. Yamamura, Y. Kawakita, K. Shibata and M. Kawai, Proton dynamics of  $\text{CsH}_2\text{PO}_4$  studied by quasi-elastic neutron scattering and PFG-NMR, *Solid State Ion.*, 2008, **179**, 2345–2349, DOI: [10.1016/j.ssi.2008.10.002](https://doi.org/10.1016/j.ssi.2008.10.002).

